J. Fluid Mech. (2008), *vol.* 610, *pp.* 69–97.
doi:10.1017/S0022112008002358 Printed in the United Kingdom

Kinematics and statistics of dense, slow granular flow through vertical channels

ANANDA K. S.†, SUDHESHNA MOKA‡ AND PRABHU R. NOTT¶

Department of Chemical Engineering, Indian Institute of Science, Bangalore 560 012, India

(Received 9 October 2007 and in revised form 10 May 2008)

We have investigated the flow of dry granular materials through vertical channels in the regime of dense slow flow using video imaging of the particles adjacent to a transparent wall. Using an image processing technique based on particle tracking velocimetry, the video movies were analysed to obtain the velocities of individual particles. Experiments were conducted in two- and three-dimensional channels. In the latter, glass beads and mustard seeds were used as model granular materials, and their translational velocities were measured. In the former, aluminium disks with a dark diametral stripe were used and their translational velocities and spin were measured. Experiments in the three-dimensional channels were conducted for a range of the channel width W, and for smooth and rough sidewalls. As in earlier studies, we find that shearing takes place predominantly in thin layers adjacent to the walls, while the rest of the material appears to move as a plug. However, there are large velocity fluctuations even in the plug, where the macroscopic deformation rate is negligibly small. The thickness of the shear layer, scaled by the particle diameter d_p, increases weakly with W/d_p. The experimental data for the velocity field are in good agreement with the Cosserat plasticity model proposed recently. We also measured the mean spin of the particles in the two-dimensional channel, and its deviation from half the vorticity. There is a clear, measurable deviation, which too is in qualitative agreement with the Cosserat plasticity model. The statistics of particle velocity and spin fluctuations in the two-dimensional channel were analysed by determining their probability distribution function, and their spatial and temporal correlation. They were all found to be broadly similar to previous observations for three-dimensional channels, but some differences are evident. The spatial correlation of the velocity fluctuations are much stronger in the two-dimensional channel, implying a pronounced solid-like motion superimposed over an uncorrelated fluid-like motion. The strong spatial correlation over large distances has led us to propose a mechanism for the production of velocity fluctuations in the absence of a macroscopic deformation rate.

1. Introduction

One of the striking phenomena in the flow of granular materials is shear localization, or the tendency of the material to shear predominantly in thin regions, while large portions remain virtually undeformed. This feature is particularly prevalent in the regime

† Present address: KLA-Tencor Software India Pvt. Ltd, Chennai India.
‡ Present address: Tata Consultancy Services Ltd, New Delhi India.
¶ Author to whom correspondence should be addressed: prnott@chemeng.iisc.ernet.in.

of dense slow flow where grain interactions are abiding, and the normal and tangential contact forces, the latter arising from Coulomb friction, are the dominant mechanisms for the transmission of stress. Though it is often stated in the literature that the thickness of the shear layer is roughly constant (about 10 grain diameters), experimental evidence contrary to this assumption has long been available (Nedderman & Laohakul 1980).

A prominent feature of dense slow granular flows is the rate-independence of the stress (Tardos, Khan & Schaeffer 1998; Albert *et al.* 1999). Another important feature, first observed by Reynolds (1885), is that deformation is usually accompanied by dilation, or reduction in the bulk density, of the material. For the continuum mechanical treatment of slow granular flows, constitutive theories for the stress, having roots in soil mechanics and metal plasticity, have been proposed, of which the critical-state theory (Schofield & Wroth 1968; Jackson 1983) is perhaps the most widely used. They are formulated to capture the features mentioned above, and have been used with some success to model flow in hoppers and bunkers (Brennen & Pearce 1978; Michalowski 1987; Prakash & Rao 1991; Cleaver & Nedderman 1993). However, these theories fail for viscometric flows; they predict that the entire material behaves as a rigid block, slipping at the walls (Tejchman & Wu 1993; Mohan, Nott & Rao 1997). For reasons that will shortly become apparent, we refer to these as the 'classical' plasticity theories.

The inability of classical plasticity theories to capture thin shear layers is due to the absence of a material length scale in the constitutive relations. Attempts to correct this deficiency have been made by treating granular materials as Cosserat continua (Mühlhaus & Vardoulakis 1987; Mühlhaus 1989; Tejchman & Gudehus 1993; Tejchman & Wu 1993), which introduces a material length scale in the constitutive relations. However, these studies addressed only the initiation of plastic flow, and posed the equations in terms of strain increments. The model was extended for sustained flow by Mohan *et al.* (1999, 2002), who developed a rigid–plastic Cosserat plasticity model, which they called the 'frictional Cosserat' model, in which the constitutive relations are posed in terms of strain rates.

The Cosserat continuum is named after Cosserat & Cosserat (1909), who first proposed the idea; it was further developed by Eringen (1968), who incorporated rotational microinertia and called it a micropolar continuum, and several other workers. Three features distinguish a Cosserat continuum: (i) the Cauchy stress tensor $\boldsymbol{\sigma}$ is, in general, asymmetric; (ii) a couple stress tensor $\boldsymbol{M}$ acts on the medium; and (iii) an additional kinematic field, namely the local spin $\boldsymbol{\omega}$ of each material point, is introduced. None of these features are present in a classical continuum: the Cauchy stress is symmetric, there is no couple stress, and the spin of a material point is not an independent variable, but is equal to the rotation rate $\boldsymbol{w}$ induced by the macroscopic velocity gradient, namely half the vorticity. Just as the Cauchy stress tensor (usually referred to simply as the stress tensor), is defined such that $\boldsymbol{n}\cdot\boldsymbol{\sigma}$ is the force per unit area on a plane of unit normal $\boldsymbol{n}$, the couple stress tensor $\boldsymbol{M}$ is defined such that $\boldsymbol{n}\cdot\boldsymbol{M}$ is the torque per unit area. For a granular material, the spin of a material point is the mean particle spin at that location. (The spin of a particle is its angular velocity with respect to a coordinate frame whose origin is at the particle centre.) As a consequence of the asymmetry of the Cauchy stress and the presence of a couple stress, the angular momentum balance, which is implicitly satisfied in a classical continuum, must be enforced in a Cosserat continuum.

Apart from the introduction of a material length scale, there is a sound fundamental reason for treating dense granular materials as Cosserat continua. It has been shown

in rather general terms that the presence of non-central interaction forces between particles lead to continuum equations of motion that represent a Cosserat continuum (McCoy, Sandler & Dahler 1966; Jenkins, Cundall & Ishibashi 1989; Lun 1991). In slow granular flows, Coulomb friction is the dominant interaction force, which is fundamentally non-central. It is therefore appropriate to model a granular material as a Cosserat continuum.

The predictions of the frictional Cosserat model of Mohan *et al.* (1999, 2002) are in good agreement with experimental data for flow in vertical channels (Nedderman & Laohakul 1980; Natarajan, Hunt & Taylor 1995) and in cylindrical Couette cells (Losert *et al.* 2000; Mueth *et al.* 2000). However, some predictions of the model have so far not been tested. For example, the deviation of $\boldsymbol{\omega}$ from $\boldsymbol{w}$ has not been measured for sustained flow. Another important prediction of the model is that the shear-layer thickness grows with the system size, though rather weakly. Nedderman & Laohakul (1980) provide some data on this point, but there were substantial measurement errors; the shear-layer thicknesses arrived at by fitting three different functional forms to the measured velocity profile are substantially different.

In this study, we have conducted flow-visualization experiments of slow granular flows in vertical channels and have made accurate measurements of the velocity profiles. We have systematically studied the effect of the channel width, wall roughness and particle roughness on the velocity field and thereby the thickness of the shear layer, and compared the data with the predictions of the frictional Cosserat model of Mohan *et al.* (1999, 2002). In addition, we have determined the mean particle spin $\boldsymbol{\omega}$ of circular disks flowing in a two-dimensional channel (i.e. a channel whose depth is only slightly greater than the thickness of the disks), and determined its deviation from half the vorticity $\boldsymbol{w}$, thereby assessing one of the key predictions of the Cosserat model. To our knowledge, this is the first study in which this kinematic Cosserat effect has been measured experimentally for sustained flow.

It is pertinent to note that some studies have reported the presence of 'wide shear zones' (Fenistein & van Hecke 2003, Fenistein, van de Meent & van Hecke 2004; Cheng *et al.* 2006) in a modified cylindrical Couette device, in which a portion of the bottom plate rotates with the inner cylinder, suggesting that it is surprising and unusual. Though the flow field in this device is interesting in itself, the presence of wide shear zones is not surprising in such a complex flow. The occurrence of shear in regions of substantial width (and far from boundaries) is known to occur in much simpler (but non-viscometric) flows, such as flow through a hopper.

The second aspect of this study is the statistics of particle velocity and spin fluctuations. Our understanding of the hydrodynamics of molecular fluids has benefited greatly from knowledge of the statistics of molecular motion. It is therefore reasonable to presume that we may derive insight into the macroscopic behaviour of granular materials by studying the statistics of particle motion. The pronounced difference in the rheological behaviour of dense granular materials and conventional fluids prompts the question of whether there is a fundamental difference in their statistical nature. In a recent study (Moka & Nott 2005), we had reported the statistics of particle velocity fluctuations of glass beads in a three-dimensional vertical channel. We had found evidence of 'universal' statistics, e.g. the probability distribution function of velocity fluctuations was found to be independent of the location in the channel, the channel width, or the wall roughness. Here, we report measurements of the statistics of translational velocity and spin fluctuations for the flow of disks in a two-dimensional channel, and compare our results with those of Moka & Nott.

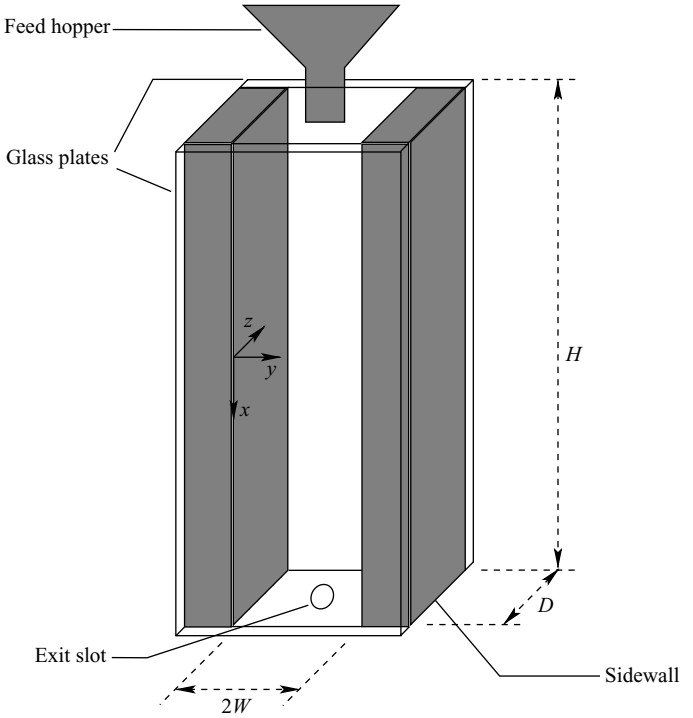

FIGURE 1. Schematic of the vertical channel used in our experiments. The front and back walls are glass plates and the sidewalls are machined aluminium bars. In some of the experiments, the inner surfaces of the sidewalls were roughened by sticking a sheet of sandpaper. The dimensions are $H = 45\,\text{cm}$, $D = 50\,\text{cm}$, and W variable for the three-dimensional channel, and $H = 96\,\text{cm}$, $D = 6\,\text{mm}$, and $W = 19\,\text{cm}$ for the two-dimensional channel. The exit slot is a circle of diameter 9 mm in the former, and a rectangle of dimensions $50 \times 6\,\text{mm}^2$ in the latter. In the two-dimensional channel, a small stretch ($\approx 10 \times 6\,\text{mm}^2$) of the base on each side of the exit slot was vibrated to disrupt arch formation.

2. Experimental set-up

For the three-dimensional channel, the flow chamber consisted of two aluminium sidewalls, and smooth, transparent glass plates used as the front and back walls (figure 1). The entire assembly was supported by a rigid metal frame, with a provision to slide the sidewalls along horizontal grooves so that width $2W$ of the channel could be changed easily. The depth D and height H of the channel were fixed. The flow was imaged through the front wall using a video camera. The channel was fed by a hopper at the top, and an aluminium plate with a circular exit slot was fastened at the bottom of the channel. The size of the exit slot determined the flow rate of the material. Glass beads of mean diameter $d_p = 0.8\,\text{mm}$, and mustard seeds of mean diameter $d_p = 1.55\,\text{mm}$ were used as model granular materials. The glass beads were coated with a shiny black pigment to improve the contrast in the images (figure 2*a*). The mustard seeds did not reflect enough light, yielding images of poor contrast from which the particles could not be clearly identified; to overcome this, a small fraction of the seeds were coated with a white pigment, which could be visualized easily (figure 2*b*). The flow was studied for smooth and rough sidewalls; the former were the bare aluminium bars, and the latter were obtained by sticking a sheet of 80 grit sandpaper to the inner surface of the bars.

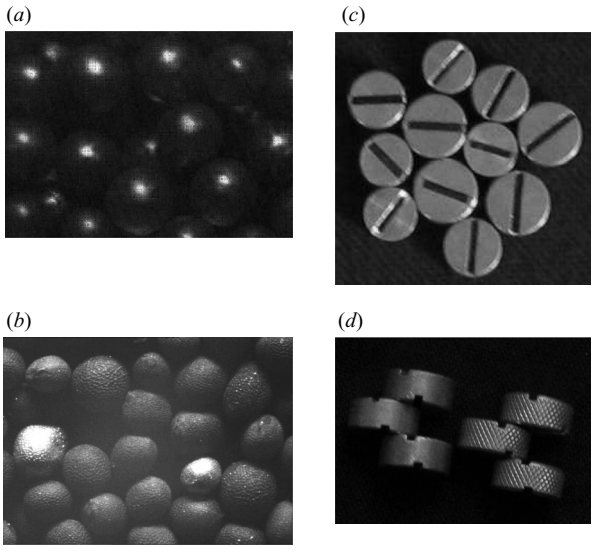

FIGURE 2. The granular materials used in the experiments. (*a*) Glass beads of mean diameter 0.8 mm used in the three-dimensional channel. The beads were coated with a shiny black pigment to improve contrast. (*b*) Mustard seeds of mean diameter 1.55 mm used in the three-dimensional channel. A small fraction of the seeds were coated with a white pigment (two of which are visible in the figure) for visualization. (*c*) Aluminium disks used in the two-dimensional channel. Dark stripes are marked in the base of the diametral grooves cut on the flat faces of the disks, to track the particle orientation. (*d*) View of the cylindrical surfaces of the disks, showing the disks with smooth and rough surfaces. The latter were obtained by knurling the surfaces. The grooves cut on the flat surfaces are clearly visible.

The two-dimensional channel was similarly constructed, except for the following differences: its depth $D = 6$ mm was only slightly higher than the thickness of the aluminium disks (5 mm) that were used as the model granular material, and the exit slot was rectangular, with length 50 mm and depth equal to D. The small clearance between the disks and the glass plates was necessary to allow smooth flow and yet maintain a monolayer of disks. The sidewalls of the channel were roughened by sticking 80 grit sandpaper. To enable the measurement of the particle spin, diametral grooves were cut on the flat surfaces of each disk, and a dark stripe was marked on the base of each groove (figure 2*c*, *d*). The stripe ended just short of the edge of the disk, so that two adjacent disks whose grooves were aligned could be be distinguished. A mixture of disks of diameter 9, 10 and 11 mm, with number fractions 0.34, 0.28 and 0.38, respectively, were used in order to avoid the crystalline order that occurs in systems of uniformly sized disks. The mean diameter of the mixture was $d_p \approx 10$ mm. To study the effect of particle roughness, the cylindrical surfaces of one batch of disks were knurled (figure 2*d*). In order to keep the flow rate low enough that the dense slow flow regime could be studied, the width of the exit slot had to be restricted to 50 mm. This, however, resulted in the formation of an arch at the exit that stopped the flow. To disrupt the formation of an arch and ensure smooth flow, an electromagnetic vibrator was used to vibrate a small stretch ($\approx$10 mm) of the base on each side of the exit slot. With the amplitude kept fixed at 0.16 mm, the lowest frequency (90 Hz) was chosen at which the arches were consistently broken. While vibration was essential to disrupt arch formation and thereby allow steady flow, the energy supplied by the vibrator was so small that it did not directly cause particle motion far from the exit.

This is substantiated by the lack of perceptible motion of the particles even 4–5 d_p above the exit slot in a static bed. Our measurements were made $\approx 50\, d_p$ above the exit slot. Thus, the only role of vibration far from the exit is to allow steady flow even when the width of the slot is small.

The particle size in the 80 grit sandpaper used to coat the walls is $\approx 200\,\mu$m. Hence, the ratio of mean grain diameter to the size of the topographical features of the wall is roughly 4 for the glass beads and 8 for the mustard seeds for the rough walls. The size of the topographical features for the machined aluminium bars is $\sim 10\,\mu$m; hence, the aforementioned ratio is ~ 100 for the smooth walls.

Particle spin was first measured in granular materials by Becker & Hauger (1982); they studied the shear of a collection of long rods in a cylindrical Couette device, with the axes of the rods parallel to that of the cylinders. They used a flexible outer cylinder that expanded to accommodate the dilation of the material upon shearing. However, their data are for very small strain; the rotation of the inner cylinder in their study was only 1.24° (as reported in Lippmann 1995). Thus, they measure a significant radial strain increment, which will be zero at steady state. More recently particle spin has been measured in cylindrical Couette flow (Howell, Behringer & Veje 1999; Mueth *et al.* 2000) and in flow down an inclined chute (Bi *et al.* 2006). Mueth *et al.* (2000) determined the mean spin profile indirectly, by requiring the velocity profiles obtained by magnetic resonence imaging (MRI) and high-speed video imaging to match; moreover, it does not appear that the mass-averaged velocity obtained by MRI can distinguish between the spin of particles and the vorticity. Howell *et al.* (1999) and Bi *et al.* (2006) measured the spin of disks by following the orientation of stripes marked on the disks, as in our study. They do not discuss the accuracy with which the stripe was painted, but the grooves in our disks were cut with machines that are used to make precision machine screws, and the accuracy of machining is greater than $100\,\mu$m, or $0.01\, d_p$. With the exception of Bi *et al.* (2006), who studied the contrasting regime of rapid flow in which particles interact by impulsive collisions, none of the above studies compared the spin with half the vorticity.

3. Image acquisition and analysis

Typical images taken during the flow of the glass beads and aluminium disks in the two- and three-dimensional channels are shown in figure 3. The acquisition of good images with adequate contrast depends crucially on the method of illumination. For glass beads, a narrow focused beam of light was ideally suited: the central part of each bead appeared as a bright spot (figure 3*a*), and the periphery was much darker. A distributed source of light resulted in multiple scattering, and therefore poor contrast. The disks in the two-dimensional channel required a very different illumination scheme, as the diametral stripe had to be distinguished from the rest of the disk. The method that worked best was diffuse lighting from the back, which helped in identifying the entire disk, and low-intensity diffuse lighting from the front, which helped in distinguishing the stripe from the rest of the disk (figure 3*b*).

The video images were acquired by a CCD camera placed in front of the channels. Three CCD cameras were used through the course of our investigation: a camera (brand unknown) with 192×144 pixels capturing 25 frames per second (f.p.s), a Basler A301fc camera with 640×480 pixels capturing 75 f.p.s. and a Kodak ES310 camera with 640×480 pixels capturing 125 f.p.s. For the two-dimensional channel, only the Kodak camera was used. The camera was mounted on a translation stage to

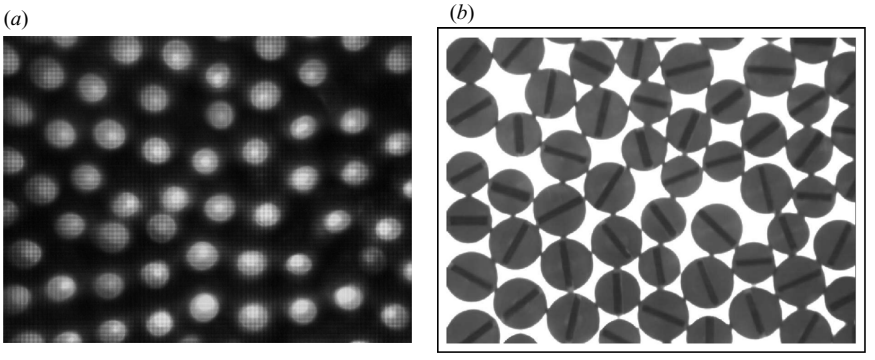

FIGURE 3. (*a*) Snapshot of the glass beads flowing in the three-dimensional channel; the bright spots are the light reflected from the central parts of the beads. The images were deliberately taken slightly out of focus to increase the size of the bright spots (cf. figure 2*a*), thereby easing particle detection. (*b*) Snapshot of the aluminium disks flowing in the two-dimensional channel; the dark lines marked on the grooves were used to measure the particle spin.

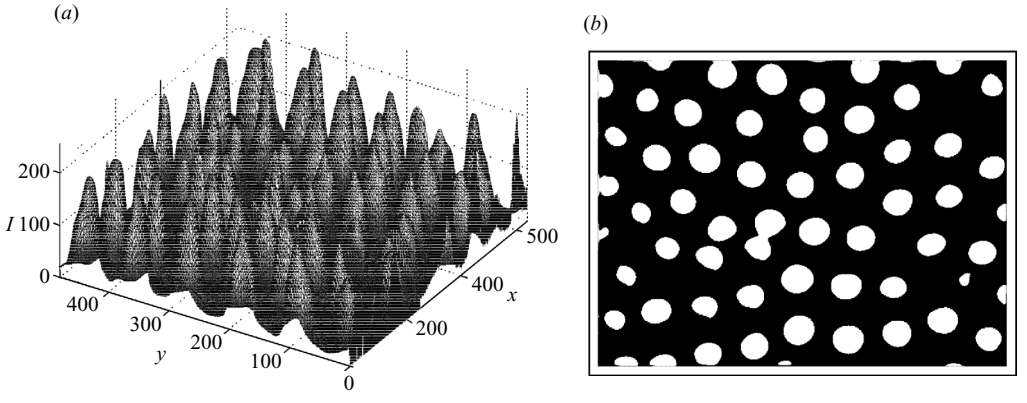

FIGURE 4. (*a*) Intensity plot for the snapshot of glass beads in figure 3(*a*). The x- and y-axes are the Cartesian coordinates, in pixels, and the z-axis is the intensity, digitized to 256 grey levels. (*b*) Thresholded image of the intensity in panel (*a*). The centroids of the white spots are taken as the centroids of the corresponding particles.

facilitate imaging at various positions in the y-direction. The movies were concurrently transferred to a computer, and the images processed subsequently.

Image analysis involved the three steps of smoothing, thresholding and particle detection (Crocker & Grier 1996; Guezennec & Kiritsis 1990). In the smoothing step, the intensity of each pixel is replaced by a weighted average of the intensity of the pixels around its centre, including itself; we used a Gaussian weighting, which rapidly decays with distance. Smoothing helps remove fluctuations in intensity introduced during acquisition, digitization, or compression of the images. In the second step, a threshold intensity is set, above which pixels are deemed to be white (intensity 1), and below which they are deemed to be black (intensity 0). Thus, thresholding converts a grey-scale image to black-and-white, thereby maximizing contrast. The choice of the threshold intensity is determined by a tradeoff between maximizing the size of the bright spots (and thereby the accuracy with which the centroid can be determined), and minimizing the frequency of merging of adjacent spots. Figure 4(*a*) shows the intensity plot for a typical image of the glass beads, and figure 4(*b*) shows

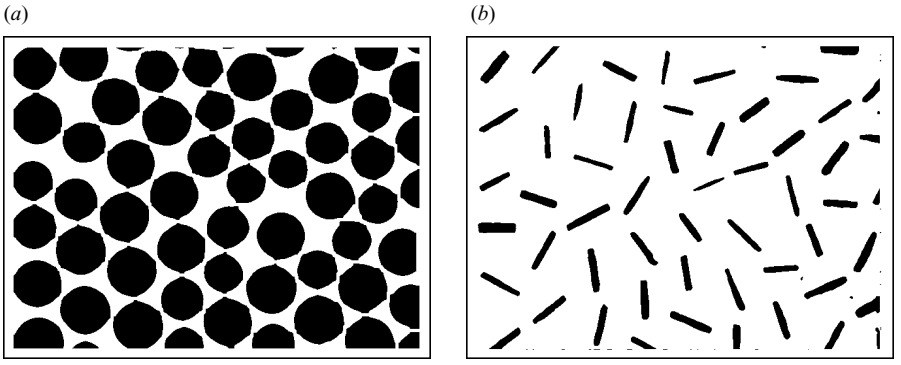

FIGURE 5. (*a*) Image of the aluminium disks flowing in the two-dimensional channel after smoothing, thresholding, segmentation and erosion. (*b*) The image of the stripes of the particles in (*a*), obtained by setting a lower threshold intensity.

its thresholded image. In the particle detection step, the particles are identified as contiguous regions of intensity 1. Only the spots whose area falls between pre-set minimum and maximum values are identified as particles, in order to filter the noise, and discard occurrences of merged spots (an instance of the latter can be seen in figure 4*b*). The centroids of the spots are determined, which are then taken to be the centres of the particles. As observed in previous studies (Moka & Nott 2005; Orpe & Kudrolli 2007), this procedure provides the particle centre with sub-pixel resolution.

The images of the disks in the two-dimensional channel required two additional steps before particle detection. In figure 3(*b*), it appears that the disks are connected by narrow 'bridges'. This is an artefact of the distributed lighting at the back, as very little light passes through the regions near the points of contact between particles. To distinguish the particles, an image segmentation, or 'watershed', algorithm (Vincent & Soille 1991) was used after the thresholding step. This creates a narrow 'channel' cutting through in the bridges. The channels were then widened by uniformly eroding the edges of the particles. The image obtained from figure 3(*b*) after thresholding, segmentation and erosion is shown in figure 5(*a*). Here, the intensity value of a black pixel is set to unity, and a white pixel to zero. The particle detection and centroid determination then proceeded as described above. The stripes on the disks were detected by setting a lower intensity threshold; the image obtained thus is shown in figure 5(*b*). The orientations of the stripes were determined by fitting an ellipse to each stripe, and determining the angle subtended by its major axis with the horizontal.

The image processing for the three-dimensional channel was performed using our own code written in C. For the two-dimensional channel, we used the software ImageJ (http://rsb.info.nih.gov/ij/); all the image-processing steps mentioned above, namely smoothing, thresholding, segmentation, erosion, centroid determination and ellipse fitting, are available either as options or plugins in ImageJ. The final result from image processing is the centroids of all the particles, and, in the case of the disks, their orientations.

The velocities of the particles were determined by the particle-tracking velocimetry (PTV) method. In this technique, the position of each particle is tracked in time and its velocity determined therefrom. In the first frame, all the identified particles are listed (Guezennec & Kiritsis 1990) and their centroids determined. The standard PTV technique uses an estimate of the local velocity to identify the expected location of a particle in the next frame, i.e. after a time δt, and searches for its centroid around the

expected location. This technique is not suitable for granular flows, owing to the large fluctuations in particle velocities. Instead, the following technique was used: given the location $\boldsymbol{r}_i \equiv (x_i, y_i)$ of the centroid of particle i in the first frame, its location in the next frame was found by searching within a circle of radius r_s centred at $\boldsymbol{r}_i$. If $r_s/\delta t$ is much greater than the maximum velocity of the particles, the position of every particle can be identified in the next frame. The velocity of the particle then is the displacement $\delta \boldsymbol{r}$ divided by the time interval δt. Similarly, the change in the orientation of the stripe of a particle between successive frames determines its spin. If particle i cannot be located within the search radius, presumably because it has moved away from the front wall, it is deleted from the list; similarly, if a particle that did not exist in the previous frame is detected, it is added to the list. We took $r_s = d_p/2$, and ensured that the maximum particle speed is significantly smaller than $r_s/\delta t$. For the glass beads imaged at 25 f.p.s. this condition sets the maximum measurable speed at 10 mm s^{-1}; the average vertical velocity of the particles was at most 3.5 mm s^{-1}, well below the maximum measurable speed. For the aluminium disks imaged at 125 f.p.s. the maximum measurable speed was 66 cm s^{-1}, while the maximum vertical velocity in our experiments was about 5 cm s^{-1}.

Profiles of the mean properties were determined by notionally dividing the channel into vertical bins of width d_p and averaging the relevant particle properties in each bin over a sufficient length of time. The mean velocity u_x, the root mean square (r.m.s.) velocity fluctuation v and the probability distribution function of velocity fluctuations f in each bin were calculated, and assigned to the mid-point of the bin. To ensure good statistics, about 9000 frames were analysed for each position (bin) in the channel.

The accuracy of the PTV method have been discussed previously (Guezennec & Kiritsis 1990; Haitao, Reeves & Louge 2004), and we therefore do not dwell on it here. As discussed in Haitao *et al.* (2004), the errors in the mean velocity are far smaller than those in the r.m.s. fluctuation velocity, as random errors sum to zero in the former, but do not in the later. We estimate that the error in the measurement of the r.m.s fluctuation velocity and spin is below 2 %, arising mainly from the presence of a velocity gradient across the bin. We could detect no variation in the data for the mean velocity profile and the probability distribution function of velocity fluctuations determined with the cameras of different speeds.

4. Experimental results

Table 1 lists the experiments that were conducted, indicating the geometry, the granular material used and the nature of the walls. As stated earlier, 'smooth walls' refer to the bare aluminium surface, and 'rough walls' to the case were the aluminium surface was coated with sandpaper. The roughness of the walls in slow flow is usually characterized by the angle of wall friction δ (Nedderman 1992, p. 40), defined as

$$\tan \delta = \frac{S}{N}, \tag{4.1}$$

where S and N are the magnitudes of the shear and normal stresses at the wall. We measured δ by placing a light metal ring (diameter 70 mm, height 20 mm) on an initially horizontal wall surface, filling it to the brim with the granular material, and slowly tilting the surface until the ring just begins to slide. The angle of wall friction δ is equal to the critical angle θ_c of the surface with the horizontal at which sliding is first detected. The angle of internal friction ϕ, which is a measure of the roughness

Experiment	Channel width ($2W$)	Granular material	W/d_p	Type of wall
E1	26.0 mm	Glass beads	16.3	Smooth
E2	36.75 mm	Glass beads	23.0	Smooth
E3	52.0 mm	Glass beads	32.5	Smooth
E4	77.25 mm	Glass beads	48.3	Smooth
E5	101.5 mm	Glass beads	63.4	Smooth
E6	26.25 mm	Glass beads	16.4	Rough
E7	37.5 mm	Glass beads	23.4	Rough
E8	50.75 mm	Glass beads	31.7	Rough
E9	75.0 mm	Glass beads	46.9	Rough
E10	102.5 mm	Glass beads	64.1	Rough
E11	37.5 mm	Glass beads	23.4	Rough
E12	68 mm	Mustard seeds	21.9	Rough
E13	38 cm	Aluminium disks	19.0	Smooth
E14	38 cm	Aluminium disks	19.0	Rough

TABLE 1. The experiments conducted.

	ϕ
Glass beads	23.3° (1.2°)
Mustard seeds	28.9° (1°)
	δ
Glass beads on smooth wall	16.6° (0.9°)
Glass beads on rough wall	21.4° (2°)
Glass beads on glass plate	16.5° (0.7°)
Mustard seeds on rough wall	23.5° (0.5°)

TABLE 2. Frictional properties of the granular materials and the walls. The average of ten independent measurements are given, with the standard deviation in parentheses.

of the granular material in the bulk (Nedderman 1992, p. 25), was measured in the same manner, but with the ring placed on a bed of granular material; ϕ is then determined from the relation $\sin\phi = \tan\theta_c$. The average of ten independent trials for each combination of granular material and wall surface are reported in table 2, with the standard deviation given in parentheses.

The method we have used to determine the angles of friction is a crude version of the Jenike shear cell (Jenike 1961), in which a normal load is applied on the material at the top of the ring, and the movement of the ring and the applied shear force are determined by displacement and force transducers. In our tests, the normal and shear stresses come from the gravitational body force, and plastic yield is detected by eye. The latter, being prone to error, may be an explanation for the deviations between repeated trials. However, such deviations are also observed in the Jenike cell and other similar instruments, and are related to the sensitivity of the material properties to its construction history, which affects the fabric, or network of contacts. The angle of friction obtained in our ring test may differ from that prevailing in the channel, because of differences in the geometry; we treat our measurements as indicative values only.

Note that the angle of friction of the glass beads on a glass plate is significant, though the latter is topographically very smooth. It is well known that surfaces that are atomically smooth (such as mica sheets) also experience a frictional force

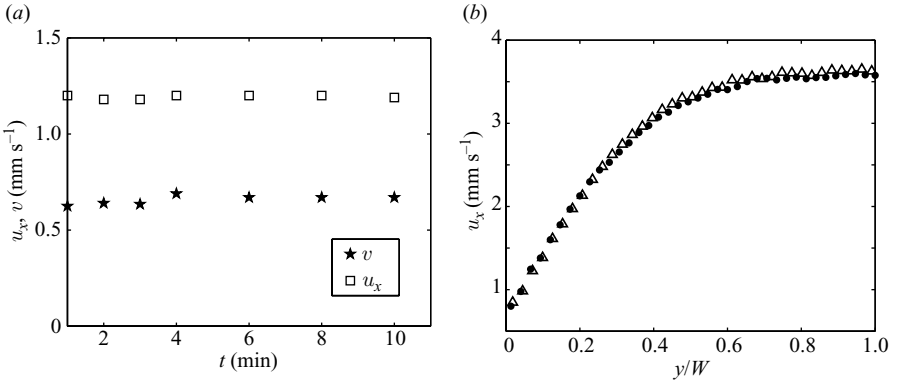

FIGURE 6. (*a*) Time evolution of the mean velocity and r.m.s. velocity fluctuation at a distance of $44.3\,d_p$ from the left-hand wall for glass beads flowing in a smooth-walled channel of half-width $W = 63.4\,d_p$ (experiment E5 in table 1). (*b*) Velocity profiles at ●, 18 cm; △, 13 cm from top, for a rough-walled channel of half-width $W/d_p = 23.4$ (experiment E7 in table 1).

when sliding over each other (Krim 1996), so the relation between the topographical roughness of a surface and its frictional properties is a complex one. For the purpose of this study, we refer to walls that offer (relatively) high friction and low friction as rough and smooth walls, respectively.

4.1. *Results for three-dimensional channels*

We first present the results for rough-walled channels. As our interest is in steady fully developed flow, image acquisition was commenced only when sufficient time elapsed after starting the flow. The initial solids fraction of the material (i.e. as poured into the channel) was roughly $\nu = 0.57$; we had no way of systematically controlling it. However, we expect the solids fraction field at steady fully developed state to be insensitive to the initial solids fraction. The time variation of the vertical mean velocity and the r.m.s. velocity fluctuation, averaged over a short time interval, is shown in figure 6(*a*). It is evident that a steady state is reached 2–3 min after the start of the flow. Figure 6(*b*) shows the velocity profile for half the channel, measured at two different heights; the profiles are almost identical, indicating that the flow is fully developed. All the data for the three-dimensional channel presented henceforth are for a distance of 18 cm from the top of the channel. Because of the symmetry of the problem about $y = W$ (some variables, such as the spin $\boldsymbol{\omega}$ and the shear stress σ_{yx} are antisymmetric), we report all variables for the left half of the channel only.

4.2. *Effect of channel width*

In figure 6(*b*), it is evident that the material moves as a plug in the core region of the channel. (We reiterate that our measurements are only for the layer of particles adjacent to the front glass wall, and hence our measurements are not for the 'true' core far from the front and back walls. A discussion on the effect of the front wall is given in § 4.5.) In conformity with previous studies (Nedderman & Laohakul 1980; Mohan *et al.* 1999; 2002), we define the dimensionless shear-layer thickness Δ as the distance from the wall, scaled by d_p, at which the velocity reaches 95 % of the velocity at the symmetry axis $u_0 \equiv u_x(y = W)$, i.e.

$$u_x(d_p\Delta) = 0.95\,u_0. \tag{4.2}$$

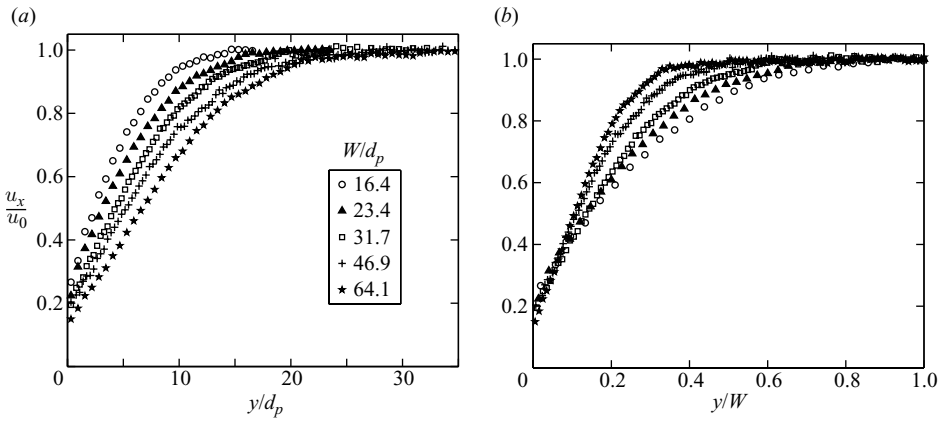

FIGURE 7. Velocity profile for glass beads, scaled by the velocity at the symmetry axis $u_0 \equiv u_x(W)$, in rough-walled channels of different width. The distance from the left wall is scaled by the particle diameter d_p in (*a*), and by the channel half-width W in (*b*).

Owing to the small spatial fluctuations in the data, we take u_0 as the average of u_x over a range of y around the symmetry axis $y = W$, within which it is roughly constant. In figure 6*b*, $\Delta = 10.3$, but it increases when the dimensionless channel width W/d_p is increased. Figure 7 shows the velocity profiles scaled by u_0 for rough-walled channels of five different widths. A systematic rise of Δ with W/d_p is evident in figure 7(*a*). However, it is also clear that Δ has only a weak dependence on W/d_p. If we plot u_x against y/W (figure 7*b*), we see that the shear layer occupies a smaller fraction of the channel as W/d_p increases; in other words, $\Delta \times (d_p/W)$ is a decreasing function of W/d_p. Another notable observation is that the slip velocity at the wall decreases as W/d_p increases. All these trends are in agreement with the prediction of the frictional Cosserat model of Mohan *et al.* (1999, 2002). Comparisons of the data with the model are made in § 4.7.

4.3. *Effect of wall roughness*

All the data presented thus far are for rough walls. A comparison of the velocity profiles of glass beads obtained for smooth and rough walls, with the channel width kept almost equal, is shown in figure 8. The thinner shear layer and higher slip velocity for the case of smooth walls is apparent. This influence of the wall roughness on the shear-layer thickness is in conformity with the observation of Nedderman & Laohakul (1980), and is also predicted by the frictional Cosserat model of Mohan *et al.* (1999, 2002), as shown in § 4.7.

The velocity profiles for smooth-walled channels of five different widths are shown in figure 9. Unlike the case of rough walls, we do not find a systematic dependence of the velocity profile on W/d_p – considering figure 9(*a*), we see that the velocity in the shear layer decreases with increasing W/d_p up to $W/d_p = 48.3$, but increases on further increasing W/d_p to 63.4. This non-monotonic variation can also be seen in figure 9(*b*). We also find the variation of Δ with W/d_p to be much weaker than in the case of rough walls. We show in § 4.7 that this difference can be explained by the frictional Cosserat model in terms of the difference in the ratio $\sin\phi/\tan\delta$ in the two cases.

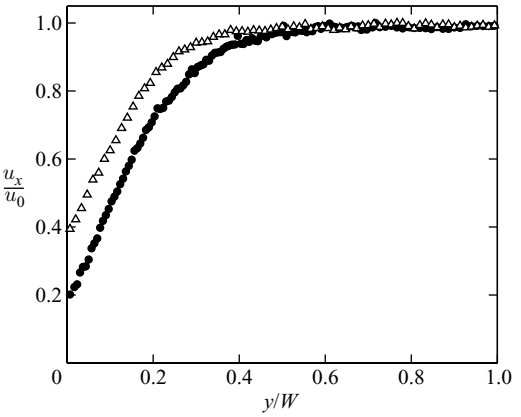

FIGURE 8. Velocity profile of glass beads in △, smooth and •, rough-walled channels of half-width $W = 48.3\,d_p$ and $46.9\,d_p$, respectively (experiments E4 and E9 in table 1).

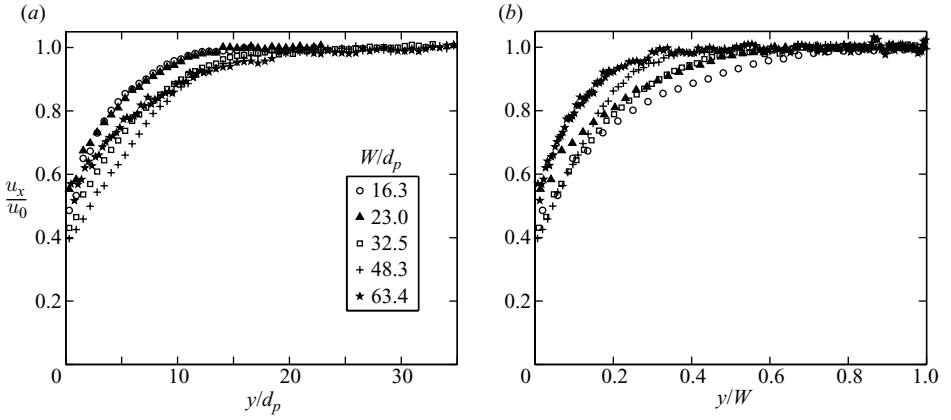

FIGURE 9. Velocity profile of glass beads in smooth-walled channels of different width. The distance from the left wall is scaled by the particle diameter d_p in (*a*), and by the channel half-width W in (*b*).

4.4. *Effect of the particle roughness*

Next, we compare the velocity profiles for the two granular materials that we have studied, namely glass beads and mustard seeds. As only a small fraction of the mustard seeds (those coated with the white pigment) could be visualized, the imaging had to be carried out for a much longer period of time to gather a sufficiently large sample of particle velocities. Hence, we examined the flow of mustard seeds for only one channel width, $W/d_p = 21.9$. We note in figure 10 that the shear layer is considerably thinner for mustard seeds. This appears counter-intuitive, as the angles of internal and wall friction for mustard seeds are higher than those of glass beads (see table 2). However, in the frictional Cosserat model it is the ratio $\sin\phi/\tan\delta$ that determines the thickness of the shear layer; the closer the ratio is to unity, the wider the shear layer. From the data for ϕ and δ in table 2, we find this ratio to be 1.009 for glass beads and 1.11 for mustard seeds. Hence the data are in qualitative agreement with the theory. A comparison of the theoretical prediction of the velocity profile with the data for mustard seeds is provided in figure 14(*a*).

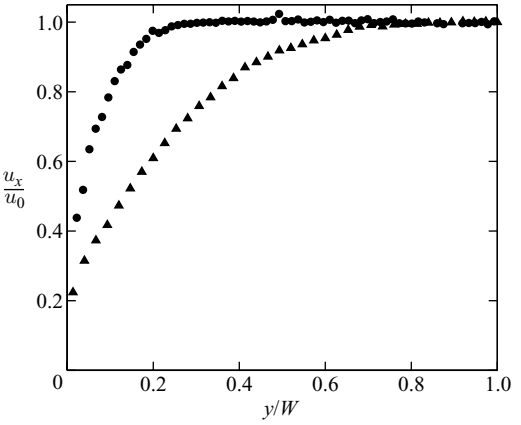

FIGURE 10. Velocity profile of ▲, glass beads and ●, mustard seeds in rough-walled channels. The dimensionless channel widths for the two cases are $W/d_p = 23.4$ and 21.9, respectively (experiments E7 and E12, respectively, in table 1).

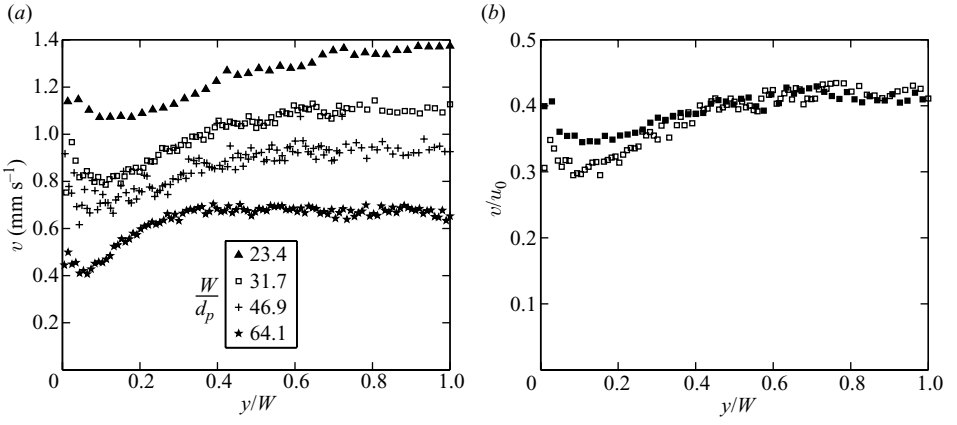

FIGURE 11. (*a*) Unscaled r.m.s velocity fluctuation profile for glass beads flowing in rough-walled channels of different width. (*b*) Comparison of the r.m.s velocity fluctuation profiles, scaled by u_0, for channels with □, rough and ■, smooth walls. The channel width for the two cases are $W/d_p = 31.7$ and 32.5, respectively.

4.5. *Velocity fluctuations*

At short time scales, we can observe in the movies that the particles execute a stick–slip motion, i.e. their velocities are not smooth functions of time. In addition, fluctuations in the particle velocity arise from fluctuations in the packing, owing to the periodic formation and collapse of small voids. These events are most probably related to the formation and collapse of force chains, or chains of particles in contact that transmit forces over distances of many d_p.

Figure 11(*a*) shows the profiles of r.m.s. fluctuation velocity v for different values of the dimensionless channel width W/d_p. In all the cases, we find v to be highest at the symmetry axis, where the gradient of mean velocity in the y-direction vanishes. However, there is probably a velocity gradient in the z-direction, owing to the frictional resistance offered by the glass walls. Though Nedderman & Laohakul (1980) report that the retardation of the particle velocity by the glass walls is less than 4 %, we

believe it is higher. This is suggested by our observation that the flow rate of the material issuing from the exit slot is roughly 20 % higher than that calculated from the velocity profile, assuming the bulk density to be constant. This suggests that the shear rate $\mathrm{d}u_x/\mathrm{d}z$ is finite adjacent to the front and back walls, and may be responsible for the velocity fluctuations in the core region. Moreover, the microstructure near the flat walls is likely to differ from that in the bulk, owing to the excluded volume-induced layering of particles. However, these considerations do not explain why v is maximum at the centre, as the shear rates in the y- and z-directions are both largest near the walls. Moreover, Orpe & Kudrolli (2007) show that substantial velocity fluctuations exist in regions far from all the walls. They imaged the motion of particles in the bulk by filling the channel with a fluid whose refractive index matched that of the particles. This method suffers from the drawback that the velocity fluctuations are damped by the fluid; indeed, fluctuations may even be caused by the fluid, owing to the long-range hydrodynamic interactions between particles. Nevertheless, it is reasonable to suppose that it provides at least a qualitative picture of the behaviour in the bulk. Thus, all the existing evidence points to the presence of substantial velocity fluctuations in regions where the macroscopic shear rate is negligibly small. The experiments of Ananda (2006) in cylindrical Couette flow also reveal similar behaviour. This is an interesting and important observation, as the thermal energy generated in a molecular fluid during flow, or the 'pseudo-thermal' energy in a granular material in the rapid flow regime, come from the stress work, which is proportional to the local shear rate. This point is discussed further in §5, where a mechanism for the generation of fluctuations in the absence of a macroscopic shear rate is proposed.

A comparison of the v profiles for smooth and rough sidewalls (figure 11*b*) is also counter to expectation – it is roughly the same in the core for the two cases, but it is higher in the shear layer for the smooth wall, though the shear rate in this case is lower (as the slip velocity is higher).

4.6. *Results for the two-dimensional channel*

We now discuss the results of our experiments of the flow of aluminium disks in the two-dimensional channel. Figure 12(*a*) shows the profiles of the mean translational velocity and the r.m.s velocity fluctuation. The velocity for the three-dimensional channel at approximately the same value of W/d_p is given for comparison. We see that the velocity varies much more sharply in the two-dimensional channel, and consequently the shear layer is considerably thinner. Another significant difference is in the velocity fluctuation (cf. figures 12*a* and 11): in the three-dimensional channel, it decreases for a short distance from the wall, and then increases to a maximum at the channel centre, whereas in the two-dimensional channel it increases for a short distance from the wall, and then decreases to a minimum at the centre. Two factors contribute to these differences: one is the stronger effect of the front and back walls on the aluminium disks in the two-dimensional channel, and the second is the additional translational and rotational degrees of freedom that the particles in the three-dimensional channel possess. It is not clear to us which of these factors dominate, and how they cause the observed differences. What is clear is that non-invasive measurement of the mean and fluctuation velocity fields far from the front and back walls is desirable.

The data in figure 12 are for the rough (knurled) aluminium disks (see figure 2*d*). We found the velocity profile of the smooth aluminium disks to be almost identical (Ananda 2006). Thus, the surface texture formed by knurling does not alter the

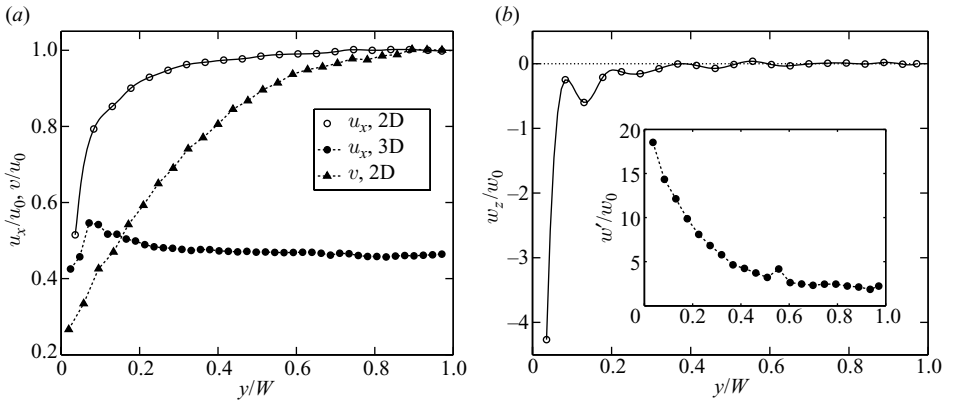

FIGURE 12. (*a*) Profiles of the mean velocity u_x and the r.m.s. fluctuation velocity v for aluminium disks in the two-dimensional channel ($W/d_p = 19$). The data for glass beads in the three-dimensional channel of similar width ($W/d_p = 16.4$) is given for comparison. The solid line passing through the u_x data for aluminium disks is a quintic spline fit. (*b*) Profiles of the mean spin ω_z and the r.m.s spin fluctuation ω' (inset) for aluminium disks in the two-dimensional channel. Both quantities are scaled by $\omega_0 \equiv u_0/W$. The solid line passing through the ω_z data for aluminium disks is a quintic spline fit.

roughness of the medium, probably because it does not lead to interlocking, or meshing, of particles in contact. All the results that follow for the two-dimensional channel are for the rough aluminium disks.

The main purpose of conducting experiments in the two-dimensional channel was to measure the particle spin. The profile of the mean spin ω_z and the r.m.s spin fluctuation ω' are given in figure 12(*b*). It is apparent that ω_z decays quickly with distance from the wall, but the variation is not monotonic; spatial oscillations of wavelength 2–3 d_p are evident. The magnitude of ω' is much larger, and it decays much more slowly with y. Thus, though the mean spin is small outside the shear layer, there are substantial spin fluctuations throughout the channel. The oscillations in the ω_z profile are a result of the 'cog-wheel' effect, i.e. particles in frictional contact rotating in opposite directions. This effect is stronger when the particles are confined to a monolayer, and is attenuated if the packing of particles is amorphous. Thus, the amplitude of the oscillations is highest near the walls, where there is excluded volume-induced order in the packing.

It was argued in §1 that a granular material in the slow flow regime behaves as a Cosserat continuum, which differs in certain ways from a classical continuum. One of the differences is that the mean spin may differ from half of the vorticity $\boldsymbol{w}$. It is therefore of interest to compare the two quantities in our experiment. As the disks are constrained to move only in the (x, y)-plane, and rotate only in the z-direction, we compare ω_z with $w_z \equiv -(\mathrm{d}u_x/\mathrm{d}y)/2$ in figure 13. The derivative of u_x was obtained from the functional form for $u_x(y)$ obtained by a spline fit of the data in figure 12(*a*). We find that w_z too decays rapidly with y and displays spatial oscillations. Note that the oscillations of ω_z and w_z are nearly in register. The spin leads the vorticity, and the difference $\omega_z - w_z$ decays with distance from the wall. We find a measurable difference between ω_z and w_z in a layer of thickness $\sim 7\, d_p$ (see figure 16*a*) from the wall. The relatively large magnitudes of ω_z and w_z at the wall obscure their variation outside the shear layer, hence an enlarged view is shown in the inset of figure 13(*b*). We believe that the constraint on the particles to reside in a single plane reduces the extent of the region over which this kinematic Cosserat effect is measurable, as

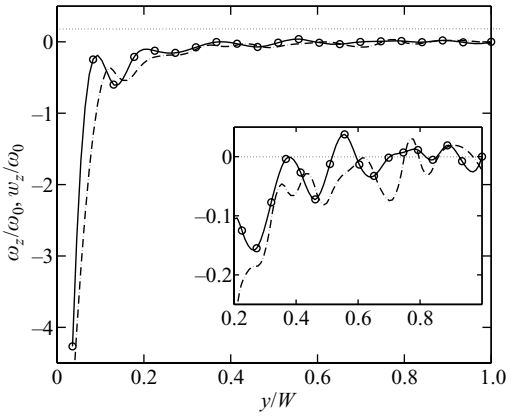

FIGURE 13. Profiles of ○, the mean spin ω_z and - · -, half the vorticity w_z (both scaled by $\omega_0 \equiv u_0/W$) for aluminium disks in the two-dimensional channel. The profile of w_z is obtained from the spline fit for $u_x(y)$ obtained in figure 12(*a*).

systems constrained to two dimensions exhibit much stronger spatial correlation (see figure 21 and the accompanying text). Though the measurement of the rotation of particles in three dimensions far from the front and back walls is an experimental challenge, it would be of significant value in assessing whether the Cosserat effects are present far from the boundaries.

4.7. *Comparison with the frictional Cosserat model of Mohan et al. (1999)*

As discussed in § 1, the predictions of the frictional Cosserat model (Mohan *et al.* 1999; 2002) were shown to be in good agreement with the data of Nedderman & Laohakul (1980) and Natarajan *et al.* (1995) for flow in vertical channels, and the data of Losert *et al.* (2000) and Mueth *et al.* (2000) for flow in cylindrical Couette cells. It is therefore of interest to compare our data with the predictions of the model.

Here, we give only the governing equations of the model, and refer to the original works for a detailed description. (Note that the governing equations below differ slightly from those in Mohan *et al.* (1999) owing to a different choice of the Cartesian reference frame.) To obtain the equations in dimensionless form, the variables are scaled in the following manner: all lengths by W, the Cauchy stress $\boldsymbol{\sigma}$ by $\rho_p g W$, the couple stress $\boldsymbol{M}$ by $\rho_p g W d_p$, the velocity $\boldsymbol{u}$ by $(gW)^{1/2}$, and the spin $\boldsymbol{\omega}$ by $(g/W)^{1/2}$. Here, ρ_p is the density of the particles, and g the gravitational body force. For steady, fully developed flow in the x-direction, and assuming no variation in the z-direction, the balances of linear momentum reduce to

$$\frac{\mathrm{d}\overline{\sigma}_{yx}}{\mathrm{d}\overline{y}} = \nu, \quad \frac{\mathrm{d}\overline{\sigma}_{yy}}{\mathrm{d}\overline{y}} = 0, \tag{4.3}$$

and the balance of angular momentum to

$$\epsilon \frac{\mathrm{d}\overline{M}_{yz}}{\mathrm{d}\overline{y}} + \overline{\sigma}_{xy} - \overline{\sigma}_{yx} = 0. \tag{4.4}$$

Here, $\epsilon \equiv d_p/W$, and the lines over the variables indicate that they are dimensionless. It is straightforward to show that the material is at a critical state (i.e. a state of isochoric motion) everywhere. The first of (4.3), together with the fact that the material is at critical state, implies that $\overline{\sigma}_{yy} = \overline{\sigma}_c(\nu) = \text{constant}$, where $\overline{\sigma}_c(\nu)$ is the dimensionless mean stress at critical state. As a result, the solids fraction ν is constant across the

channel. This is a deficiency of the model, as it is well known (Natarajan *et al.* 1995; Mueth *et al.* 2000) that the solids fraction is lower in the shear layer than in the plug.

The momentum balances are supplemented by the yield condition

$$a_1\left(\overline{\sigma}_{xy}^2+\overline{\sigma}_{yx}^2\right)+2\,a_2\,\overline{\sigma}_{xy}\overline{\sigma}_{yx}+\frac{\overline{M}_{yz}^2}{L^2}=(\overline{\sigma}_c\sin\phi)^2. \tag{4.5}$$

Here, L is a mesoscopic length scale (scaled by d_p), and a_1 and a_2 are dimensionless constants (but only the ratio $A\equiv a_2/a_1$ is of relevance).

Equations (4.3)–(4.5), with boundary conditions

$$\frac{\overline{\sigma}_{yx}}{\overline{\sigma}_{yy}}=-\tan\delta \quad \text{at } \overline{y}=0, \tag{4.6}$$

$$\overline{\sigma}_{xy}=0,\quad \overline{\sigma}_{yx}=0 \quad \text{at } \overline{y}=1. \tag{4.7}$$

fully determine the stress fields. Boundary condition (4.6) is the friction boundary condition at the wall (Nedderman 1992, p. 40; Mohan *et al.* 1999), and (4.7) is due to the symmetry of the flow about the plane $y=W$ (see Mohan *et al.* 1999).

The kinematic variables are determined by the flow rule, which relate the strain rate and stress tensors. Mohan *et al.* (1999, 2002) used the associated flow rule, which for the problem at hand reduces to

$$\frac{\mathrm{d}\overline{u}_x}{\mathrm{d}\overline{y}}=-\frac{(1+A)(\overline{\sigma}_{xy}+\overline{\sigma}_{yx})\,\overline{\omega}_z}{\overline{\sigma}_{xy}+A\overline{\sigma}_{yx}}, \tag{4.8}$$

$$\frac{\mathrm{d}\overline{\omega}_z}{\mathrm{d}\overline{y}}=-\frac{2(1+A)\,\overline{M}_{yz}\,\overline{\omega}_z}{\epsilon L^2(\overline{\sigma}_{xy}+A\overline{\sigma}_{yx})}. \tag{4.9}$$

The $\overline{u}_x$ and $\overline{\omega}_z$ fields are obtained by solving (4.8) and (4.9), using the solution of the stress fields already obtained, and the boundary conditions

$$\overline{u}_x=-\epsilon K\,\overline{\omega}_z \quad \text{at } \overline{y}=0, \tag{4.10}$$

$$\overline{\omega}_z=0 \quad \text{at } \overline{y}=1. \tag{4.11}$$

Boundary condition (4.10) is the kinematic boundary condition proposed by Mohan *et al.* (1999), relating the slip velocity and the particle spin at the wall, and (4.11) is a statement of the antisymmetry of ω_z about $y=W$. Though it is desirable, we do not have a micromechanical model relating the constant K to the topographic features of the wall.

The particular forms of the yield condition and the flow rule chosen above are only to obtain a qualitative understanding of the frictional Cosserat model, and for simplicity of the analysis. There is evidence that the Mohr–Coulomb yield condition and a non-associated flow rule may be more suitable for granular materials. However, the extension of the model to incorporate these refinements is straightforward.

The method of solution of (4.3)–(4.11) is discussed in Mohan *et al.* (1999). We shall now compare the model predictions with our experimental data. It is readily deduced from (4.3)–(4.5) that all components of the stress and couple stress are proportional to $\overline{\sigma}_c(\nu)$. Since the flow rule involves only ratios of the stress components, the value of the solids fraction ν does not affect the kinematic variables. Similarly, it is easily seen from (4.8)–(4.11) that all the kinematic variables can be determined only to within an arbitrary multiplicative factor. This factor is set by the flow rate, which the model cannot determine unless we consider the flow in the region close to the exit slot. However, when scaled by the velocity at the symmetry axis u_0, the velocity profile is

uniquely determined for a given set of parameters ϵ, ϕ, δ L, K and A. Similarly, the spin profile is uniquely determined if scaled by u_0/W. We shall therefore compare the experimental and theoretical profiles scaled in this manner. The parameter $\epsilon \equiv d_p/W$ is set by the size of the channel and particles, and the parameters ϕ and δ were measured independently for each set of particles and walls (see table 2). We do not vary A, but keep it fixed at 1/3, as in the studies of Tejchman & Wu (1993) and Mohan *et al.* (l999, 2002). The only parameters that we use to fit the model predictions to the data are K and L.

For glass beads flowing in rough-walled channels, the values $L = 20$ and $K = 3.6$ provide a good fit of the velocity data for $W = 64.1\, d_p$. (The fit was judged by eye – we did not attempt a systematic least-squares procedure to obtain the best fit.) The above value of L was retained for all channel widths, for smooth and rough walls. The value of K determines only the slip velocity, not the overall shape of the velocity profile. For glass beads flowing in smooth-walled channels, $K = 9.2$ matched the slip velocity for $W = 63.4\, d_p$, which was retained for all the other channel widths. Mohan *et al.* (2002) showed that $L = 10$ fits the data of Mueth *et al.* (2000) for mustard seeds in cylindrical Couette flow; we retained the same value and used $K = 3.6$ for determining the theoretical prediction for mustard seeds flowing in a rough-walled channel.

Mohan *et al.* (1999) found $L = 10$ to provide a good fit for the data of Nedderman & Laohakul (1980) and Natarajan *et al.* (1995) for the flow of glass beads in vertical channels. A reason for the significantly larger value of L required for fitting our data could be the coating of the glass beads; the shiny black pigment seems to render the particle surface smoother. However, the relation between L and the micromechanics of particle interactions is an open issue, and it is far from clear why a smoother surface should lead to an increase in the mesoscopic length scale.

Comparisons of the predicted velocity profiles with the data for glass beads and mustard seeds are shown in figure 14. Considering first the results for glass beads, it is clear that there is good agreement in general, but there is a slight difference which grows as W/d_p decreases. The agreement is not so good for mustard seeds – the theory predicts a significantly thicker shear layer. A better fit may be achieved if a smaller value is chosen for L, but we refrain from doing so for the reason mentioned above. In all the cases, the predicted slip velocity at the wall agrees quite well with the data, suggesting that the kinematic boundary condition (4.10) with constant K may be an accurate representation.

Figure 15 shows the variation of the dimensionless shear-layer thickness Δ, defined in (4.2), with W/d_p. The values determined from the velocity profiles obtained experimentally (symbols) for glass beads are shown alongside the predictions of the frictional Cosserat model for rough and smooth walls. In both cases, there is good qualitative agreement – it is clear that Δ grows with W/d_p, but it is also clear that the growth is weak. In quantitative terms, the model under-predicts Δ slightly for small W/d_p.

In the asymptotic limit $W/d_p \to \infty$, the Cosserat model predicts the following scaling for Δ (Mohan *et al.* 1999):

$$\Delta = \begin{cases} 1.498\, \dfrac{\gamma L}{2(\beta\gamma - 1)} & \tan\delta < \sin\phi, \\ 1.275\, (L^2/2)^{1/3}\, (W/d_p)^{1/3} & \tan\delta = \sin\phi, \end{cases} \tag{4.12}$$

where $\beta \equiv \sin\phi/\tan\delta$, $\gamma \equiv \beta + (\beta^2 - 1)^{1/2}$. (Mohan *et al.* (1999) used the symbol N in place of β, but since N is often used to denote the normal stress, we use the latter in

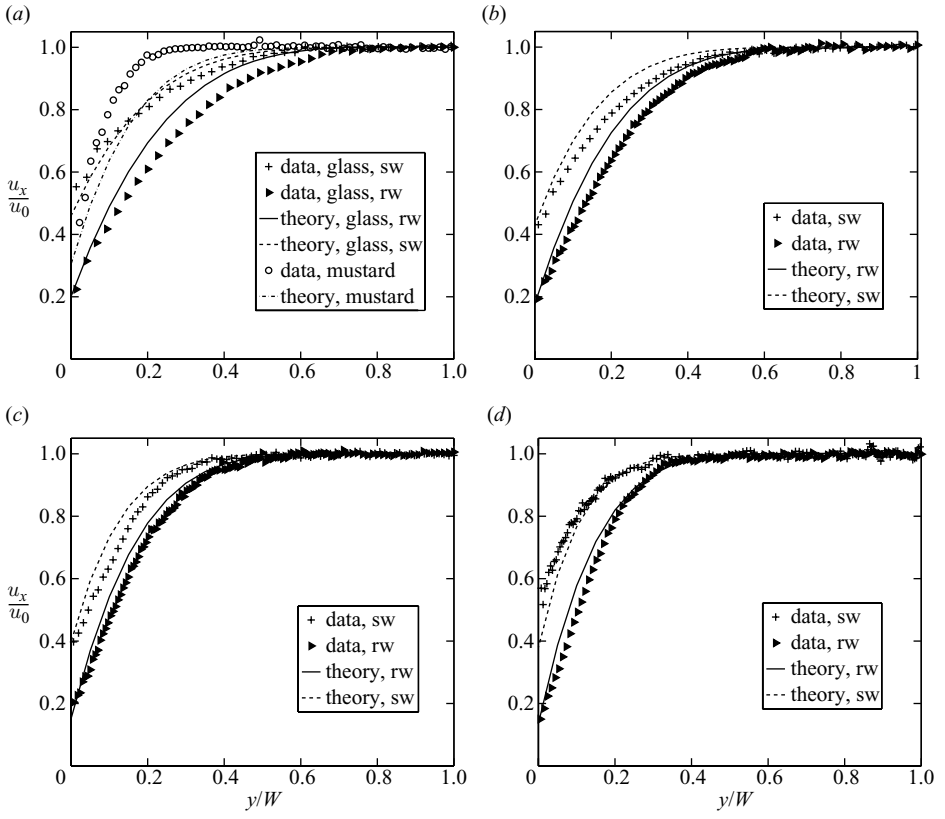

FIGURE 14. Comparison of the predictions of the frictional Cosserat model with our experimental data for the flow of glass beads and mustard seeds in smooth, and rough-walled channels. sw, smooth walls; rw, rough walls. (*a*) The channel width for glass beads are $W/d_p = 23$ (sw) and 23.4 (rw), and for mustard seeds is 21.9 (rw). (*b*) $W/d_p = 32.5$ (sw) and 31.7 (rw). (*c*) $W/d_p = 48.3$ (sw) and 46.9 (rw). (*d*) $W/d_p = 63.4$ (sw) and 64.1 (rw).

this work.) The case of $\tan\delta = \sin\phi$ is usually referred to as the condition of 'fully rough walls'. From our measurements of ϕ and δ (see table 2), we find that for glass beads $\beta = 1.01$ for rough-walled channels, and $\beta = 1.33$ for smooth-walled channels. The higher slope of the data for rough walls infigure 15 is in agreement with the above prediction.

We next compare the predictions of the spin and vorticity profiles with our experimental data. For the theory, we have used the parameters ϕ, δ, L and K for glass beads in a rough-walled channel, as the values for a monolayer of aluminium disks are not known. Moreover, we are only interested in a qualitative comparison, as the measurements are for a two-dimensional channel while the theory is for a three-dimensional channel of infinite extent in the z-direction. We see in figure 16 that the predictions qualitatively resemble our observations. The spin leads the vorticity, and both fall off with distance from the wall, though the decay is significantly faster in the data. A difference between the model predictions and the experimental data is that ω_z and w_z vary smoothly in the model, while small spatial oscillations in ω_z are observed in the data. As mentioned in § 4.6, the faster decay and the oscillations are at least partly a result of confinement of the particles to a monolayer.

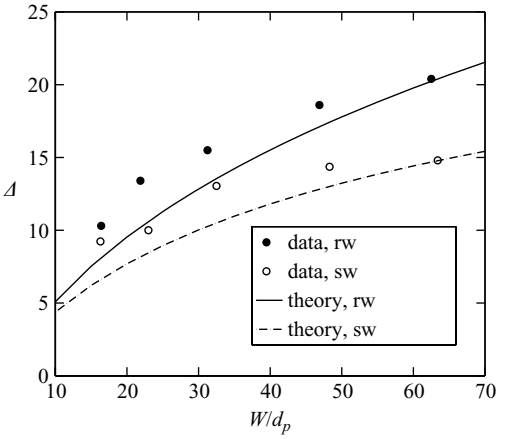

FIGURE 15. Effect of channel width on shear layer thickness Δ (see (4.2) for definition) for glass beads flowing in smooth- and rough-walled channels. The theoretical prediction is derived for the parameter values $L = 20$, and $K = 9.2$ and 3.6 for smooth and rough walls, respectively.

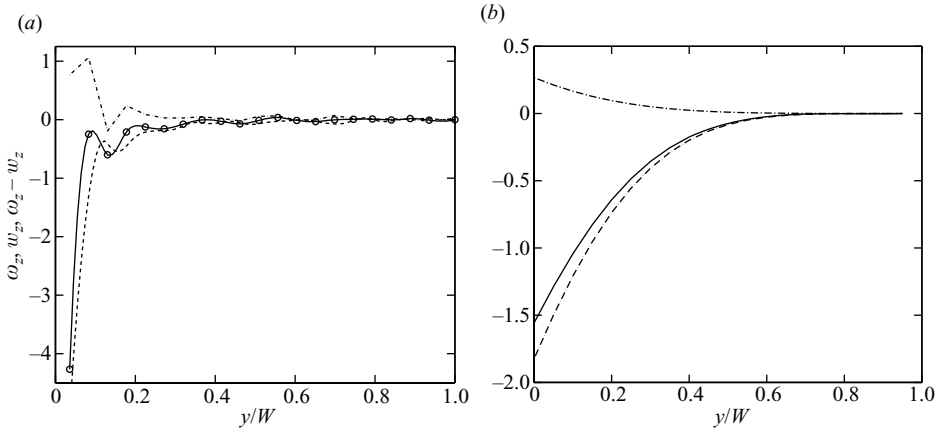

FIGURE 16. Profiles of ○, the spin $\overline{\omega}_z$, - - -, half the vorticity $\overline{w}_z \equiv -(\mathrm{d}\overline{u}_x/\mathrm{d}\overline{y})/2$, and -·-, their difference, all scaled by u_0/W. (*a*) Data from the two-dimensional channel. (*b*) Predictions of the same by the frictional Cosserat model.

Although the stresses were not measured in this study, the predictions of the model are shown in figure 17 to provide a qualitative feel of is main features. A thorough study of the effect of the model parameters on the stress fields may be found in Mohan *et al.* (1999). The parameter values used here are the same as in figure 16, but results for both smooth and rough walls are given. The solids fraction is determined by (4.6), and therefore depends on the wall roughness. However, its values for the smooth and rough walls differ so little that $\overline{\sigma}_{yx}$ is almost identical in the two cases. A substantial difference between $\overline{\sigma}_{yx}$ and $\overline{\sigma}_{xy}$ is evident in figure 17(*a*). Figure 17(*b*) shows that the couple stress $\overline{M}_{yz}$ is negative, and its magnitude increases with distance from the wall; its slope vanishes at the symmetry axis, as required by the boundary conditions (4.7) in conjunction with the angular momentum balance (4.4).

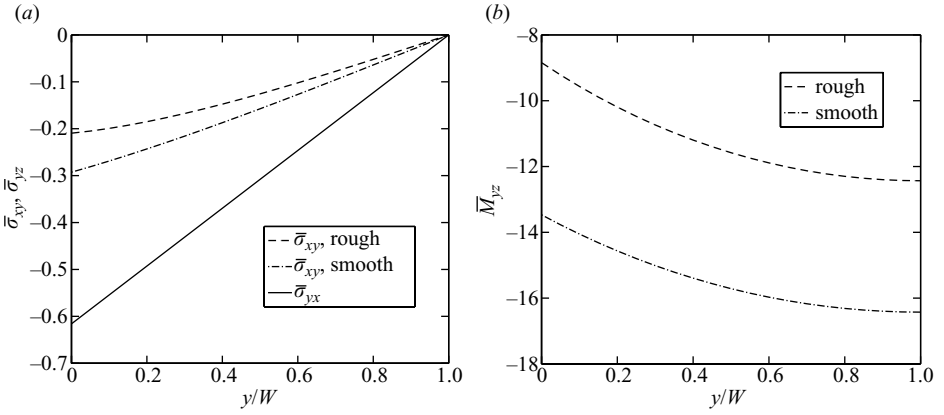

FIGURE 17. Predictions of the frictional Cosserat model of (*a*) the shear stresses $\overline{\sigma}_{xy}$ and $\overline{\sigma}_{yx}$ and (*b*) the couple stress $\overline{M}_{yz}$ for smooth- and rough-walled channels. See text for parameter values.

5. Statistics of particle velocity and spin

As stated in §1, our motivation for studying the statistics of particle velocity is to make a connection between the microscopic particle dynamics and the macroscopic rheological response of the material. This connection has been made for simple molecular fluids, and to an extent, even in complex fluids such as polymer solutions and melts. There is clearly a marked difference in the way dense granular materials and conventional fluids respond to applied forces, and one of the questions is whether there is also a fundamental difference in their statistical nature. Molecular fluids are close to thermodynamic equilibrium even when subjected to very large shear rates, but granular flows are fundamentally far from equilibrium, as particles have no fluctuational motion in the absence of forcing. As a result, the probability distribution function (PDF) of particle velocity fluctuations in molecular fluids is very close to the Maxwell–Boltzmann distribution, but *a priori* we do not expect this to be the case for dense granular flows. We also expect the PDF for the latter to depend on the shear rate, as that is what provides energy for the fluctuations.

Moka & Nott (2005) reported experimental measurements of the statistics of particle velocity fluctuations in dense granular flow through three-dimensional vertical channels. Their main findings were that the PDF of particle velocity fluctuations is non-Maxwellian, anisotropic, and follows a power law at large velocities, in agreement with the first expectation above. Remarkably, the second expectation was shown to be incorrect: the PDFs are identical in the shear layer and the core, when the velocity fluctuation is suitably normalized; there is almost no macroscopic deformation rate in the core, and we therefore expect the nature of fluctuations there to be different, if not absent altogether. The spatial correlation of the velocity fluctuations suggests a mechanism for the generation of fluctuations even in the absence of shear (Moka & Nott 2005), as discussed below.

In this section, we discuss our measurements of the statistics of fluctuations in the translational velocity and spin in two-dimensional channels, and compare our results with that of three-dimensional channels. The distribution of velocities in the x- and y-directions (see figure 1) were determined as a function of position in the channel. Defining the scaled velocity fluctuation in the x-direction $\xi_x \equiv (c_x - u_x)/v$, the probability distribution function $f_x(\xi_x)$ is determined by making a histogram of the

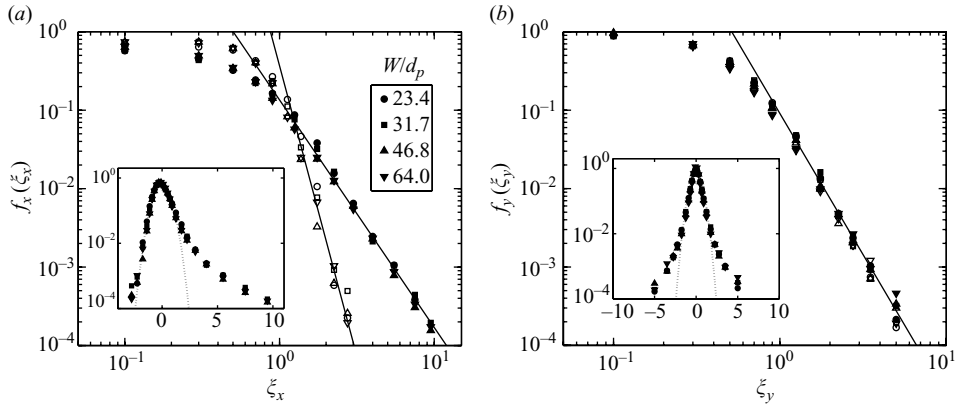

FIGURE 18. Probability distribution function for (*a*) vertical, and (*b*) horizontal particle velocity fluctuations in the shear layer. Filled symbols represent positive fluctuations, open symbols represent negative fluctuations, and the dotted line in the inset graph is the Maxwell–Boltzmann distribution with the same variance. The straight lines are fits of the data for large velocity fluctuations, showing power law decay of the PDF. Data from Moka & Nott (2005). © 2005 the American Physical Society.

number distribution of ξ_x, and normalizing it so that $\int f_x(\xi_x)\,\mathrm{d}\xi_x = 1$. The distribution function $f_y(\xi_y)$ for horizontal velocities is determined similarly. This is done for each bin (see §3) in the channel.

To place our results in context, we have shown in figure 18 the data of Moka & Nott (2005) for the PDF at a location within the shear layer for glass beads flowing in rough-walled three-dimensional channels. A few important features of the PDF are apparent. (i) We note that $f_x(\xi_x)$ is not symmetric about $\xi_x = 0$ (figure 18*a*) – the decay of f_x is more rapid for negative ξ_x than for positive values. Thus, it appears that gravity induces a preference for large downward velocity fluctuations. (ii) $f_y(\xi_y)$ is symmetric about $\xi_y = 0$, as there is no preferred direction for horizontal velocities. (iii) In both directions, the PDF decays as a power law, $f_i(\xi_i) \sim |\xi_i|^{-n}$, when $|\xi_i|$ is sufficiently large. (iv) Perhaps one of the most surprising features is that the PDFs for all the channel widths collapse into a single curve. In addition, Moka & Nott (2005) found that the PDFs are identical in the shear layer and the core; indeed, within the region of fully developed flow, it is virtually independent of the position in the channel. Thus, although v varies across the channel, and $v(y)$ depends on W/d_p (see figure 11), the distribution of the fluctuation velocity scaled by v appears to be universal.

Orpe & Kudrolli (2007) found agreement with some key aspects of the results of Moka & Nott (2005); they too found that the velocity distribution has a power-law tail. However, they also observed some differences; they found $f_x(\xi_x)$ to be symmetric about zero, but Moka & Nott (2005) found it to be distinctly asymmetric. It is not clear how these difference are related to the presence of a retarding wall in our study, and a viscous suspending liquid in theirs, but they point to the need for the non-invasive measurement of velocity fluctuations far from the walls using a method that does not require a suspending liquid, such as magnetic resonance imaging.

We now consider the PDF for the flow of aluminium disks in the two-dimensional channel. The PDF is presented in figure 19, where the data of Moka & Nott (2005) for a three-dimensional channel of width $W/d_p = 23.4$ is given for comparison. The rough trends in the two cases are similar, but some differences are apparent. There is an

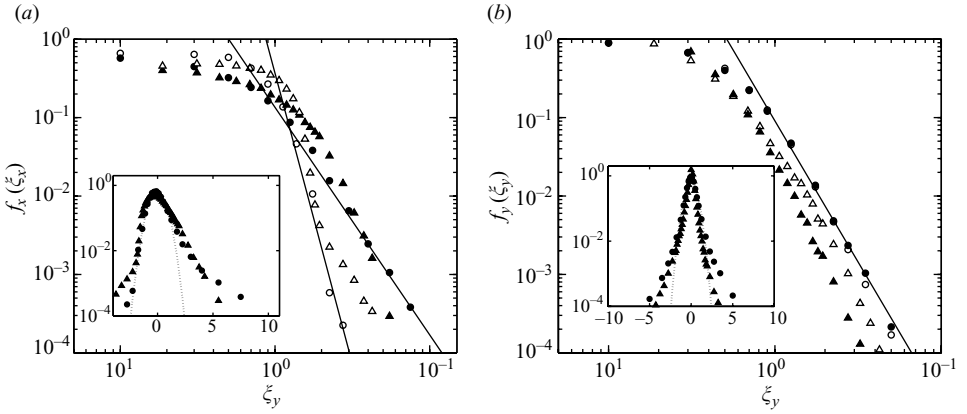

FIGURE 19. Comparison of the probability distribution function of velocity fluctuations in the ▲, two- and ●, three-dimensional channels for (*a*) vertical, and (*b*) horizontal velocity fluctuations. Filled symbols represent positive fluctuations, and open symbols represent negative fluctuations. The dotted line in each inset represents the Maxwell–Boltzmann distribution with the same variance. Data for the three-dimensional channel ($W/d_p = 23.4$) are from Moka & Nott (2005). The straight lines represent the power-law fits obtained by Moka & Nott (see figure 18).

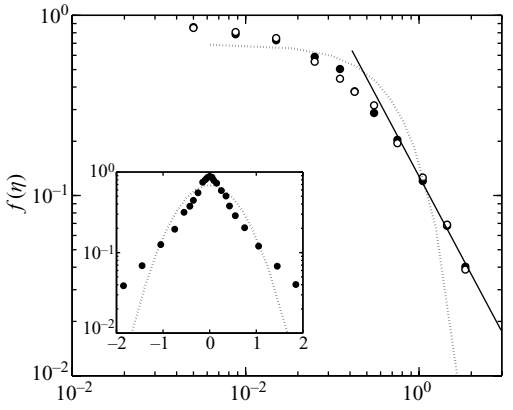

FIGURE 20. Probability distribution function of particle spin fluctuations. Filled symbols represent positive fluctuations, and open symbols represent negative fluctuations. The dotted line represents the Maxwell–Boltzmann distribution with the same variance. The straight line is the power-law fit of the data for large $|\eta|$.

asymmetry in the distribution of ξ_x about $\xi_x = 0$, and the PDF deviates significantly from the Maxwellian, but we cannot discern a power-law tail. The PDF of ξ_y is roughly symmetric about $\xi_y = 0$, and appears to have a power-law tail of roughly the same exponent as in the three-dimensional channel, but the value of f_y at large $|\xi_y|$ is lower.

The PDF of particle spin fluctuations in the two-dimensional channel (figure 20) is almost perfectly symmetric about zero, and deviates significantly from the Maxwellian. The symmetry about $\eta = 0$ is expected, as there is no preferred direction for spin fluctuations. For the limited range of spin fluctuations that we were able to measure, there appears to be a power-law tail. Howell *et al.* (1999) had measured the PDF of

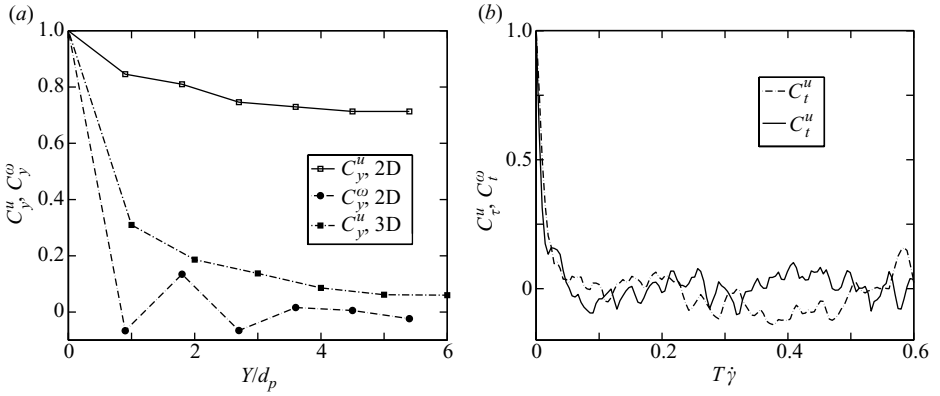

FIGURE 21. (*a*) Spatial correlation functions of the translational velocity and spin fluctuations for the two-dimensional channel. The results of Moka & Nott (2005) for a three-dimensional channel of width $W/d_p = 23.4$ is shown for comparison. (*b*) Time correlation function of the translational velocity and spin fluctuations for the two-dimensional channel. Time is scaled by the inverse of the local shear rate $\dot{\gamma} \equiv \mathrm{d}u_x/\mathrm{d}y$.

spin in cylindrical Couette flow, but their data differ qualitatively from ours: they found a distinct asymmetry in the PDF about $\eta = 0$, and the decay is not of the form of a power law, but has a more complicated structure. Part of the difference may be because the disks in their experiment were supported on a horizontal surface, whose retardation must have been significant, but we are unable to explain the asymmetry in their distribution of spin.

We now consider the spatial and temporal correlation functions of the velocity fluctuations. These functions throw light on the nature of deformation of the material. The spatial correlation function of any property p over a separation $\boldsymbol{R}$ is defined as

$$C_r^p(\boldsymbol{R}) \equiv \frac{\langle p'(t, \boldsymbol{r})\, p'(t, \boldsymbol{r}+\boldsymbol{R})\rangle}{\langle p'(t, \boldsymbol{r})^2\rangle}, \tag{5.1}$$

where $p'(t, \boldsymbol{r})$ is fluctuation in p at position $\boldsymbol{r}$, i.e. the difference between its instantaneous value and its long-time average at the same location. The angle brackets indicate an average over all pairs of particles separated by a distance $\boldsymbol{R}$; if the system is in a statistically steady state (as is the case in our experiments), the averaging may be done over time. Here, we only consider the spatial correlation of u_x and ω_z with distance Y in the y-direction, and denote them as $C_y^u(Y)$ and $C_y^\omega(Y)$, respectively. Figure 21(*a*) shows the two quantities for the two-dimensional channel, with the data of Moka & Nott (2005) for a three-dimensional channel of width $W/d_p = 23.4$ shown for comparison. In all the cases, the reference point y is the mid-point of the shear layer. Considering $C_y^u(Y)$ first, we note that it decays with Y, but not to zero. Thus, a correlated solid-like motion of the particles is superimposed over the uncorrelated fluid-like motion. However, the degree of correlation is much higher in the two-dimensional channel. This provides an explanation for the shear layer being thinner in the two-dimensional channel (see figure 12). In contrast, the decay of $C_y^\omega(Y)$ to zero shows that spin fluctuations are not correlated over long distances.

The correlation of property p over a time interval T is measured by the time correlation function

$$C_t^p(T) \equiv \frac{\langle p'(t, y)\, p'(t+T, y)\rangle}{\langle p'(t, y)^2\rangle}. \tag{5.2}$$

Unlike the spatial correlation, we determined the time correlation for the velocity and spin averaged over the particles in a bin, not for the velocities of individual particles. This is because the particles could not be tracked for distances greater than the frame size. Figure 21(*b*) shows that the fluctuations become uncorrelated very quickly.

We believe that the strong spatial correlation of the translation velocity, implying solid-like motion, is a result of the stick–slip (Budny 1979; Nasuno *et al.* 1998), or jamming–unjamming, phenomena that is known to exist in dense granular flows. This leads to an explanation for the presence of velocity fluctuations in the core (see figure 11) where the macroscopic shear rate is negligibly small. We believe that when the medium is released, or unjammed, during the slip phase, the unbalanced force accelerates the particles for a short period of time. The kinetic energy acquired by the particles is partly dissipated as true thermal energy (heat) and partly converted to fluctuational modes in the next stick or jammed phase. This cycle occurs repeatedly, maintaining a steady state. The rapid decay of the time correlation to zero indicates that the stick–slip motion itself is uncorrelated beyond a short time scale.

Orpe & Kudrolli (2007) measured $C_y^u(Y)$ in the core, but far from the front and back walls, and found that it drops to a roughly constant plateau for $Y > 2d_p$. Though their value of $C_y^u(Y)$ in the plateau is significantly smaller than what we observe, it is nevertheless finite, supporting our above hypothesis on the generation of velocity fluctuations in the absence of a macroscopic shear rate.

6. Summary and conclusions

We have studied experimentally the flow of model granular materials through vertical channels in two- and three-dimensional channels, by video imaging and particle tracking. In both types of channels, the translational velocity of each particle was determined by tracking its centroid. In the two-dimensional channel, the spin of each disk was determined by tracking the orientation of the diametral stripe marked on its flat surfaces. From the velocity and spin of each particle, the profiles of the mean velocity u_x and spin ω_z fields, and the r.m.s fluctuations of the velocity v and spin ω' were determined. The velocity profiles were determined for a range of the channel width W, in order to assess the effect of W on the shear-layer thickness. In addition, certain statistical properties of the velocity and spin fluctuations were examined.

As in previous studies on dense granular flows, we find that the material shears only in thin layers adjacent to the walls, while the core region near the centre moves as a plug. Contrary to popular belief, the thickness of the shear layer is not a constant, but grows with the channel width. This result is in agreement with the prediction of the frictional Cosserat model of Mohan *et al.* (1999, 2002). The shear-layer thickness $d_p\Delta$ grows weakly with W/d_p, where d_p is the particle diameter, which is also a prediction of the model. The model involves two parameters, namely the slip coefficient K and the mesoscopic length L; these were chosen by obtaining a fit with the measured velocity profile for the widest channel with smooth and rough walls. A slight deviation of the model prediction from the data is seen for smaller W/d_p, but overall there is good agreement.

An important, and surprising, observation in our investigation is the presence of relatively large velocity fluctuations in the channel core, where the macroscopic shear rate $\mathrm{d}u_x/\mathrm{d}y$ is virtually zero. For all the values of W/d_p, the profile of v shows a minimum near the wall, and a maximum at the channel centre, $y = W$ (see figure 11). One explanation for the generation of fluctuational motion in the core could be that there is a finite velocity gradient in the z-direction, and the stress work $\sigma_{zx} \times (\mathrm{d}u_x/\mathrm{d}z)$

is dissipated as fluctuational kinetic energy. However, this does not explain why v is maximum at the centre, as the shear rates in the y- and z-directions are largest near the walls. A more plausible explanation for the generation of velocity fluctuations is suggested by the behaviour of the spatial correlation of velocity fluctuations, discussed below. This observation casts doubt on the conventional notion that the central core of the channel moves as a solid plug, suffering no deformation – it indicates that there are fluctuations in the deformation rate, though the time-averaged deformation rate may be vanishingly small.

One of the important features of a Cosserat continuum is the deviation of $\boldsymbol{\omega}$ from half the vorticity $\boldsymbol{w}$. We determined the z-component of this difference in the two-dimensional channel from the measured profiles of ω_z and u_x, and found it to be significant in a layer of thickness $\sim 7\,d_p$ from the walls. The spin leads the vorticity, and the difference $\omega_z - w_z$ decreases with distance from the wall, though small spatial oscillations render the variation non-monotonic. The thickness of the layer over which the vorticity and spin are significant is lower than that predicted by the model. We believe that the confinement of the particles to a monolayer reduces the thickness of this layer and causes the spatial oscillations, owing to the strong spatial correlations that are observed in two-dimensional systems.

The second aspect of our study is the statistics of particle velocity and spin fluctuations. The probability distribution function (PDF) of velocity fluctuations in the two-dimensional channel is found to be roughly similar to that observed by Moka & Nott (2005) for three-dimensional channels, but some differences are evident. As in Moka & Nott, the PDF of velocity fluctuations in the x (flow)-direction is not symmetric about zero, it is roughly symmetric for the y (gradient)-direction, and departs significantly from the Maxwellian for both directions. We do not discern a power-law tail in the PDF of the velocities in the x-direction, but it appears close to a power law in the y-direction. The PDF of spin fluctuations is symmetric about zero, and appears to decay as a power law.

The spatial correlation of velocity fluctuations is much stronger in the two-dimensional channel than in three-dimensional channels, implying that solid-like motion is more prevalent in the former. This provides an explanation for the thinner shear layer in the two-dimensional channel. However, the spatial correlation of spin decays rapidly with the separation distance to zero. The time correlation of velocity and spin fluctuations also decay quickly. We infer from these observations that the deformation is not smooth and continuous, but occurs by repetitive stick–slip, or jamming–unjamming transitions. As argued by Moka & Nott (2005), this suggests a plausible mechanism for the generation of fluctuations even in the absence of a macroscopic shear rate: during each slip or unjamming phase, there is an unbalanced force which results in a momentary and localized acceleration, and the kinetic energy gained is transferred to fluctuational modes in the next stick phase.

Our findings have a bearing on some models that have been proposed for the rheology of slow dense granular flows. Savage (1998) proposed a model in which he argued that the strain rate at any location fluctuates in time, with a standard deviation ϵ, and determined the macroscopic stress tensor $\langle \boldsymbol{\sigma} \rangle$ by computing its average over a distribution of strain rates. To achieve closure, he assumed that ϵ is proportional to the granular temperature T, which is determined by a balance for the fluctuational kinetic theory, derived from kinetic theory. In light of our results, it appears that the idea of accounting for fluctuations in the strain rate has merit. However, we do not believe that ϵ is directly related to T, as we observe large fluctuations even in the core, where the stress work resulting from the macroscopic strain rate is negligibly

small. Moreover, an energy balance derived for the rapid flow regime, where grain inertia determines all interactions, is not appropriate for the regime of dense slow flow. Some other studies, such as Mohan *et al.* (1997), have assumed that material is below the threshold of plastic yield. This too appears untenable when there are significant velocity fluctuations within the core.

Thus, while it is desirable to incorporate strain-rate fluctuations in a rheological model, a better understanding of the correlation between the fluctuations in the stress and fluctuations in the velocity and strain rate is required. On the experimental front, non-invasive imaging of particle motion in the bulk, i.e. far from the walls would go a long way to building an understanding of the kinematics and statistics.

We are grateful to Mr Mahadeva Rao for his help in setting up the experimental apparatus, and to Professor Sanjeev Kumar Gupta for lending us his video camera. We have benefited from many discussions with Proffesor Kesava Rao through the course of our investigation. We acknowledge financial support from the Department of Science and Technology and the Indo-French Centre for the Promotion of Advanced Research.

REFERENCES

Albert, R., Pfeifer, M. A., Barabasi, A. & Schiffer, P. 1999 Slow drag in a granular medium. *Phys. Rev. Lett.* **82**, 205–208.

Ananda, K. S. 2006 Kinematics and statistics of dense granular flows. Master's thesis, Indian Institute of Science.

Becker, M. & Hauger, W. 1982 Granular material – an experimental realization of a plastic Cosserat continuum? In *Proc. Intl. Symp. Mechanics of Inelastic Media and Structures*, pp. 23–39. Warszawa–Poznan.

Bi, W., Delannay, R., Richard, P. & Valance, A. 2006 Experimental study of two-dimensional, monodisperse, frictional-collisional granular flows down an inclined chute. *Phys. Fluids* **18**, 123302.

Brennen, C. & Pearce, J. C. 1978 Granular material flow in two dimensional hoppers. *Trans. ASME J. Appl. Mech.* **45**, 43–50.

Budny, T. J. 1979 Stick-slip friction as a method of powder flow characterization. *Powder Technol.* **23**, 197–201.

Cheng, X., Lechman, J. B., Fernandez-Barbero, A., Grest, G. S., Jaeger, H. M., Karczmar, G. S., Möbius, M. E. & Nagel, S. R. 2006 Three-dimensional shear in granular flow. *Phys. Rev. Lett.* **96**, 038001.

Cleaver, J. A. S. & Nedderman, R. M. 1993 Theoretical prediction of stress and velocity profiles in conical hoppers. *Chem. Engng Sci.* **48**, 3693–3702.

Cosserat, E. & Cosserat, F. 1909 *Theorie des Corps Deformables*. A. Hermann, Paris.

Crocker, J. C. & Grier, D. G. 1996 Methods of digital video microscopy for colloidal studies. *J. Colloid Interface Sci.* **179**, 298–310.

Eringen, A. C. 1968 Theory of micropolar elasticity. In *Fracture*, vol. 1 (ed. H. Liebowitz). Academic.

Fenistein, D. & van Hecke, M. 2003 Universal and wide shear zones in granular bulk flow. *Nature* **425**, 256.

Fenistein, D., van de Meent, J. W. & van Hecke, M. 2004 Universal and wide shear zones in granular bulk flow. *Phys. Rev. Lett.* **92**, 094301.

Guezennec, Y. G. & Kiritsis, N. 1990 Statistical investigation of errors in particle image velocimetry. *Exps. Fluids* **10**, 138–146.

Haitao, X., Reeves, A. P. & Louge, M. Y. 2004 Measurement errors in the mean and fluctuation velocities of spherical grains from a computer analysis of digital images. *Rev. Sci. Instrum.* **75**, 811–818.

Howell, D. W., Behringer, R. P. & Veje, C. T. 1999 Fluctuations in granular media. *Chaos* **9**, 559–572.

Jackson, R. 1983 Some mathematical and physical aspects of continuum models for the motion of the granular materials. In *Theory of Dispersed Multiphase Flow* (ed. R. E. Meyer), pp. 291–337. Academic.

Jenike, A. W. 1961 Gravity flow of bulk solids. *Tech. Rep.* Bulletin 108. University of Utah Engineering Experiment Station.

Jenkins, J. T., Cundall, P. A. & Ishibashi, I. 1989 Micromechanical modeling of granular materials with the assistance of experiments and numerical simulations. In *Powders and Grains* (ed. J. Biarez & R. Gourvès), pp. 257–264. A. A. Balkema.

Krim, J. 1996 Friction at the atomic scale. *Sci. Am.* **275**, 48–56.

Lippmann, H. 1995 Cosserat plasticity and plastic spin. *Appl. Mech. Rev.* **48**, 753–762.

Losert, W., Bocquet, L., Lubensky, T. C. & Gollub, J. P. 2000 Particle dynamics in sheared granular matter. *Phys. Rev. Lett.* **85**, 1428–1431.

Lun, C. K. K. 1991 Kinetic theory for granular flow of dense, slightly inelastic, slightly rough spheres. *J. Fluid Mech.* **233**, 539–559.

McCoy, B. J., Sandler, S. I. & Dahler, J. S. 1966 Transport properties of polyatomic fluids. IV. The kinetic theory of a dense gas of perfectly rough spheres. *J. Chem. Phys* **45**, 3485–3512.

Michalowski, R. L. 1987 Flow of granular media through a plane parallel/converging bunker. *Chem. Engng Sci.* **42**, 2587–2596.

Mohan, L. S., Nott, P. R. & Rao, K. K. 1997 Fully developed flow of coarse granular materials through a vertical channel. *Chem. Engng Sci.* **52**, 913–933.

Mohan, L. S., Nott, P. R. & Rao, K. K. 1999 A frictional Cosserat model for the flow of granular materials through a vertical channel. *Acta Mech.* **138**, 75–96.

Mohan, L. S., Rao, K. K. & Nott, P. R. 2002 A frictional Cosserat model for the slow shearing of granular materials. *J. Fluid Mech.* **457**, 377–409.

Moka, S. & Nott, P. R. 2005 Statistics of particle velocities in dense granular flows. *Phys. Rev. Lett.* **95**, 068003.

Mueth, D. M., Debregeas, G. F., Karczmar, G. S., Eng, P. J., Nagel, S. R. & Jaeger, H. M. 2000 Signatures of granular microstructure in dense shear flows. *Nature* **406**, 385–389.

Mühlhaus, H. B. 1989 Application of Cosserat theory in numerical solution of limit load problems. *Ing. Arch.* **59**, 124–137.

Mühlhaus, H. B. & Vardoulakis, I. 1987 The thickness of shear bands in granular materials. *Géotechnique* **37**, 271–283.

Nasuno, S., Kudrolli, A., Bak, A. & Gollub, J. P. 1998 Time-resolved studies of stick–slip friction in sheared granular layers. *Phys. Rev.* E **58**, 2161–2171.

Natarajan, V. V. R., Hunt, M. L. & Taylor, E. D. 1995 Local measurements of velocity fluctuations and diffusion coefficients for a granular material flow. *J. Fluid Mech.* **304**, 1–25.

Nedderman, R. M. 1992 *Statics and Kinematics of Granular Materials*. Cambridge University Press.

Nedderman, R. M. & Laohakul, C. 1980 The thickness of shear zone of flowing granular materials. *Powder Technol.* **25**, 91–100.

Orpe, A. V. & Kudrolli, A. 2007 Velocity correlations in dense granular flows observed with internal imaging. *Phys. Rev. Lett.* **98**, 238001.

Prakash, J. R. & Rao, K. K. 1991 Steady compressible flow of cohesionless granular materials through a wedge-shaped bunker. *J. Fluid Mech.* **225**, 21–80.

Reynolds, O. 1885 On the dilatancy of media composed of rigid particles in contact. With experimental illustrations. *Phil. Mag.* **20**, 469–481.

Savage, S. B. 1998 Analyses of slow high-concentration flows of granular materials. *J. Fluid Mech.* **377**, 1–26.

Schofield, A. N. & Wroth, C. P. 1968 *Critical State Soil Mechanics*. McGraw-Hill.

Tardos, G. I., Khan, M. I. & Schaeffer, D. G. 1998 Forces on a slowly rotating, rough cylinder in a Couette device containing a dry, frictional powder. *Phys. Fluids* **10**, 335–341.

Tejchman, J. & Gudehus, G. 1993 Silo-music and silo-quake experiments and a numerical Cosserat approach. *Powder Technol.* **76**, 201–212.

Tejchman, J. & Wu, W. 1993 Numerical study of patterning of shear bands in a Cosserat continuum. *Acta Mech.* **99**, 61–74.

Vincent, L. & Soille, P. 1991 Watersheds in digital spaces: an efficient algorithm based on immersion simulations. *IEEE Trans. Pattern Anal. Machine Intell.* **13**, 583–598.